A self-consistent field study of diblock copolymer/charged particle system morphologies for nanofiltration membranes

Bo Zhang, Xianggui Ye, and Brian J. Edwards[a)]
Materials Research and Innovation Laboratory (MRAIL), Department of Chemical and Biomolecular Engineering, University of Tennessee, Knoxville, Tennessee 37996, USA

(Received 26 August 2013; accepted 5 December 2013; published online 27 December 2013)

A combination of self-consistent field theory and density functional theory was used to examine the stable, 3-dimensional equilibrium morphologies formed by diblock copolymers with a tethered nanoparticle attached either between the two blocks or at the end of one of the blocks. Both neutral and interacting particles were examined, with and without favorable/unfavorable energetic potentials between the particles and the block segments. The phase diagrams of the various systems were constructed, allowing the identification of three types of ordered mesophases composed of lamellae, hexagonally packed cylinders, and spheroids. In particular, we examined the conditions under which the mesophases could be generated wherein the tethered particles were primarily located within the interface between the two blocks of the copolymer. Key factors influencing these properties were determined to be the particle position along the diblock chain, the interaction potentials of the blocks and particles, the block copolymer composition, and molecular weight of the copolymer. © *2013 AIP Publishing LLC*. [http://dx.doi.org/10.1063/1.4851375]

I. INTRODUCTION

Nanofiltration is an emerging technology with a wide range of technical applications, including oil processing, separation, and concentration of amino acids, waste water treatment, and many others.[1,2] The key benefit of nanofiltration membranes over other available types of separation processes (such as ultrafiltration and reverse osmosis) is their capability to retain small molecules and ions, both organic and inorganic, at high throughput levels; hence steric exclusion is an important factor in their application. However, another important factor to their extensive application in the separations and purification industries is their ability to retain molecules and ions based on charge, i.e., the so-called "Donnan exclusion."[3,4] Several types of nanofiltration membranes, both organic and inorganic, have been developed and produced on an industrial scale, such as zeolite membranes, titanium dioxide membranes, polyamide membranes, sulfonated polymer membranes, etc.[5–8]

The pore size and charge distribution (surface charge density) are two key factors affecting the performance of nanofiltration membranes. Furthermore, an effective nanofiltration membrane should also remain insoluble in the operating environment, possess a low thickness, and be mechanically, chemically, and thermally stable.[9] Useful methods of nanofiltration membrane preparation nowadays include interfacial polymerization, surface modification, layer-by-layer self-assembly, and so on. However, these can be very complex processes; e.g., interfacial polymerization depends on many conditions, such as the chemical properties of the monomer and solvent, pH, temperature, concentration of monomer, and phase transfer catalysis, which lead to control and consistency issues in industrial manufacture.[7] Another method of nanofiltration membrane production is using hydrophilizing agents (sulfuric, hydrochloric, nitric, and phosphoric acids) to modify reverse osmosis membranes. However, the mechanical properties are generally adversely affected during the modification.[10]

In 1991, layer-by-layer self-assembly technology was first developed by Decher to prepare nanofiltration membranes through alternating assembly of anionic and cationic layers.[11] Self-assembly of block copolymers (BCP) with nanoparticles (NP) also provides a promising means to construct nanofiltration membranes, since the BCP-NP system can self-assemble into an enormous range of interesting nanoscale morphologies.[12,13] In a copolymer system composed of two immiscible blocks, lamellar, cylindrical, bicontinuous, and spherical long-range morphologies have been observed.[12] The nanoscale dimensions of the morphological characteristics of these BCP membranes makes them viable candidates for nanofiltration membranes, once one of the blocks has been removed via chemical or thermal degradation.[13,14] Indeed, it is well known that the length scales of the inherent structural characteristics can be finely tuned via modification of the molecular weight and interaction potentials between the two blocks, thus providing direct parameters that can be used to tailor size exclusion into possible membrane applications. Furthermore, the incorporation of charged particles into the membrane self-assembly adds the possibility of tuning the charge exclusion to specific applications, thus complementing the size exclusion effect.

Mixtures of particles and copolymers can lead to formation of many complex mesophases, depending on such factors as particle size, chemical properties of the particles and blocks, external field, volume fraction of a given

a)Author to whom correspondence should be addressed. Electronic mail: bje@utk.edu

 © 2013 AIP Publishing LLC

block, etc.[15,16] In practice, researchers have characterized the self-assembled BCP-NP system for both inorganic (Si, Au) and organic (polyhedral oligomeric silsesquioxane POSS) molecules.[17,18] The polystyrene capped gold system has been studied in both aqueous and organic media for a wide range of chain lengths. These studies demonstrated that a very uniform particle distribution could be produced throughout the film.[18] A block copolymer tethered with POSS can form arrays of cylindrical channels (radii of approximately 9 nm) by spin coating on a silicon substrate and then exposing to solvent vapor.[14] The location and orientation of charged nanoparticles in the polymer matrix can also be controlled by their selectivity and size, opening up a large number of potential applications.[19]

To meet the demanding technological applications of nanofiltration membranes, it will ultimately be necessary to be able to tailor specific membranes to provide the desired balance of both steric and charge exclusion for particular systems. Much experimental effort is currently being expended in this area following the intuitive pathways described above, but very little theoretical guidance is available to allow a systematic approach toward future directed membrane self-assembly. Many theoretical tools have been developed over the past few decades that possess great potential for describing the BCP-NP system, such as molecular Brownian dynamics,[20] Monte Carlo,[21–23] hybrid field theory,[24,25] dissipative particle dynamics,[26,27] and self-consistent field theory.[28,29] The real-space, self-consistent field theory (SCFT) is a powerful technique that has proven successful for discovering and predicting morphologies of complex copolymers, both in bulk and in solution. Thompson *et al.* have developed a "SCFT/DFT" approach that combines self-consistent field theory for the blocks with density functional theory (DFT) for the particles to examine hybrid composite morphologies.[30,31] Recent theoretical research along these lines has demonstrated that these BCP-NP systems can self-assemble into a variety of interesting morphologies with variable particle distributions concentrated at the interfaces between the distinct polymer-rich regions of the self-assembled structure.[23–25,31–33] Tethering neutral nanoparticles to one end of the BCP chain directs additional self-assembled structures, including several types of micellar structures, such as rod-like micelles, vesicles, and sphere-like micelles.[20,25,33–35]

Zhu *et al.*[35] performed mainly 2-dimensional simulations of BCP-NP systems with a nanoparticle tethered to one end of the BCP chain. Two cases were studied, one in which the particles were neutral to both blocks of the BCP, and one in which the particles disfavored both of the blocks. In cases where a neutral nanoparticle (P) was tethered to the B block of an AB copolymer, three distinct long-range ordered structures were observed. At constant particle radius, when the volume fraction of the A block (f_A) is low, the ABP molecules pack into a hexagonal array of A-rich cylinders surrounded by a B-rich matrix, which preferentially contains the majority of the particles. At intermediate values of f_A, lamellar phases are formed, again with the nanoparticles preferentially located in the B-domains. At high values of f_A, a narrow region of B-rich cylinders is present, and again the nanoparticles are mostly confined to the B-rich domains (i.e., the cylinders). Changing the particle radius had no effect on the qualitative characteristics of the phase diagram, although increasing particle size tended to narrow the f_A-range of all three ordered phases. When the interactions of the nanoparticles were unfavorable to both blocks of the BCP, a wider range of ordered structures was observed. Of particular interest are cases where the particles formed hexagonal arrays of cylindrical domains within a matrix of the AB copolymer and lamellar structures where particle-rich cylinders were located within the B-rich domains. Zhu *et al.* also performed several fully 3D simulations, apparently corroborating in these cases the extension of their equilibrated 2D morphologies to 3-dimensional space, although additional domains of nanospheres arranged in cubic and quasi-face-centered cubic structures were also noted. However, for many points within the investigated parameter space, it is not clear how the restriction to 2D simulations affected the resulting phase diagrams.

The purpose of this article is to examine the phase diagrams of BCP-NP systems in which the nanoparticles are tethered either between the two blocks or at the end of one of the blocks using a combination of self-consistent field theory and density functional theory, as described by Thompson *et al.*[30,31] The nanoparticles are allowed to interact (via a standard interaction potential) with neither or both blocks of the copolymer (both favorably and unfavorably), and the stable equilibrium morphologies are obtained via a suite of 3-dimensional simulations. Phase diagrams of the equilibrium morphologies are constructed, of a similar nature to those of Zhu *et al.*,[35] and are compared with their results in the overlapping cases to validate our simulations and to explore the differences between their 2D and our 3D simulations. Using these phase diagrams, identification of several key parameter ranges (in terms of molecular weight of the blocks, interaction potentials, nanoparticle position along the BCP chain, etc.) are identified that might serve as a guide to future morphological tailoring studies of nanofiltration membranes. Our primary goal is to determine parameter ranges wherein one can obtain morphologies that are amenable to applications in nanofiltration membrane technology, such as cylinders of one component of the BCP arrayed within a matrix of the other, with a heavy concentration of nanoparticles at the interface between the two phases. Selective thermal or chemical degradation of the cylindrical BCP component could then lead to a membrane of charged nanotubes, tailoring both steric and charge exclusion to potential nanofiltration membrane applications.[13,14]

II. THEORETICAL METHODS

We examine two BCP-NP systems: (a) the particle is tethered at the free end of the B block of the copolymer (ABP), and (b) the particle is tethered between the two blocks (APB). The free energy of the system is expressed using the framework of SCFT/DFT with interaction parameters quantifying the affinities between the blocks and particles. These parameters are denoted using $\chi_{AB}N$ and $\chi_{iP}N$ (i = A or B), where χ_{AB} is a binary interaction potential of the Flory-Huggins type between dissimilar monomers and N is the total

TABLE I. Interaction parameters between blocks and particles for the target systems.

System	ABP-N	ABP-AP	ABP-BP	APB-N	APB-AP
$\chi_{AP}N$	0.0	30.0	− 30.0	0.0	30.0
$\chi_{BP}N$	0.0	− 30.0	30.0	0.0	− 30.0

number of monomers per chain. The quantity χ_{AB} is positive and describes the degree of incompatibility (immiscibility) of the two blocks of the BCP. In this study, we have assumed typical ranges for this interaction parameter in the five target systems (described below) that were examined using SCFT/DFT simulations, i.e., $\chi_{AB}N \in [8, 28]$ in dimensionless units.[16,28,31,33,35–43] The interaction parameters between the particles and blocks, $\chi_{iP}N$, are assumed to be short-ranged and of the Flory-Huggins type, i.e., negative when the particles favor a particular block, and positive when they disfavor a block. This type of short-range interaction potential has been assumed in prior Dissipative Particle Dynamics studies of charged polymer membranes (e.g., see Ref. 44) where the effects of atomistic potentials, such as Lennard-Jones and Coulombic, are coarse-grained into Flory-Huggins type of mesoscopic interaction parameters. Hence the interactions of charged particles on diblock film morphology are primarily steric (excluded volume) and energetic (particle surface interactions with neighboring chain segments), both being short-ranged interactions at the mesoscale. Hence, modeling the particle interactions using Flory-Huggins type parameters should provide a reasonable estimation of these interactions for the types of block copolymers used for nanofiltration membranes, where charge susceptible polymer backbone chains are undesirable. The values of the $\chi_{iP}N$ assumed for the target systems are presented in Table I. These values were chosen based on those assumed by Zhu *et al.*[35]

We chose five target systems to study in our 3-dimensional simulations, with the corresponding interaction parameter values defined in Table I. The first of these corresponds to the case examined in two dimensions by Zhu *et al.*,[35] that of neutral, end-tethered nanoparticles (ABP-N), which can be used to validate our 3D simulations and to determine differences between these and the 2D simulations of Zhu *et al.* We also examined the following four cases: (1) particles tethered to the end of the B-block which disfavor the A-block and favor the B-block (ABP-AP); (2) particles tethered to the end of the B-block which disfavor the B-block and favor the A-block (ABP-BP); (3) neutral particles tethered between the two blocks (APB-N); and (4) particles tethered between the two blocks that disfavor the A-block and favor the B-block (APB-AP). (Note that APB-BP was not examined since it is symmetric with the APB-AP case.) These systems were targeted because together they describe all combinations of charged-species interactions with the possible blocks of the BCP.

The radius of a spherical hard particle, R_P, is set to 0.33 R_g, where R_g is the unperturbed mean-square radius of gyration of the copolymer chain. This value was chosen since it is the lowest value of this parameter examined by Zhu *et al.*, where the various regions of the phase diagrams are the widest—see Fig. 3 of Ref. 35. For a given system volume, V, the variable f denotes the overall volume fraction of the AB copolymer chain, and f_P represents the overall particle volume fraction. According to the assigned value of R_P ($0.33R_g$), $f_P = 0.035$. We denote as f_A and f_B the volume fractions of the A and B blocks of the polymer chain. Thus we have $f \cdot (f_A + f_B) + f_P = 1$.

In the framework of the SCFT/DFT method, the dimensionless free energy F (relative to $N_C k_B T$, where N_C is the number of chains, k_B is Boltzmann's constant, and T is the absolute temperature) of an ABP or APB system is given by the expression [28–31]

$$\begin{aligned} F = &-\ln\left(\frac{Q}{V}\right) + \frac{1}{V}\int d\mathbf{r}[\chi_{AB}N\phi_A(\mathbf{r})\phi_B(\mathbf{r}) + \chi_{AP}N\phi_A(\mathbf{r})\phi_P(\mathbf{r}) + \chi_{BP}N\phi_B(\mathbf{r})\phi_P(\mathbf{r}) \\ &- w_A(\mathbf{r})\phi_A(\mathbf{r}) - w_B(\mathbf{r})\phi_B(\mathbf{r}) - w_P(\mathbf{r})\rho_P(\mathbf{r}) \\ &- \xi(\mathbf{r})(1 - \phi_A(\mathbf{r}) - \phi_B(\mathbf{r}) - \phi_P(\mathbf{r})) + \rho_P(\mathbf{r})\psi_{HS}(\bar{\phi}_p(\mathbf{r}))]. \end{aligned} \quad (1)$$

Here $\phi_A(\mathbf{r})$, $\phi_B(\mathbf{r})$, and $\phi_P(\mathbf{r})$ are the local volume fractions of the A-block, B-block, and the particles. Also, $\xi(\mathbf{r})$ is the Lagrange multiplier that is used to ensure the incompressibility condition, $\chi_{ij}N$ quantifies the interaction between components i and j, and $\rho_P(\mathbf{r})$ is the distribution of particle centers. The local particle volume fraction, $\phi_P(\mathbf{r})$, is expressed as

$$\phi_P(\mathbf{r}) = \frac{1-f}{V_R}\int_{|\mathbf{r}'|<R_P} d\mathbf{r}'\rho_P(\mathbf{r}+\mathbf{r}'), \quad (2)$$

and the weighted nonlocal volume fraction of particles, $\bar{\phi}_P(\mathbf{r})$, is given by

$$\bar{\phi}_P(\mathbf{r}) = \frac{1-f}{V_{2R}}\int_{|\mathbf{r}'|<2R_P} d\mathbf{r}'\rho_P(\mathbf{r}+\mathbf{r}'). \quad (3)$$

In the above expressions, V_R is the volume of a sphere with radius R_P, and V_{2R} is the volume of a sphere with radius $2R_P$. ψ_{HS} quantifies the steric energy of the particles according to a modified Carnahan-Starling equation for a hard-sphere fluid[45]

$$\psi_{HS}(\bar{\phi}_P) = \frac{4\bar{\phi}_P(\mathbf{r}) - 3\bar{\phi}_P(\mathbf{r})^2}{(1-\bar{\phi}_P(\mathbf{r}))^2}. \quad (4)$$

The symbol Q in Eq. (1) is the partition function, defined as

$$Q = \int d\mathbf{r}\, q(\mathbf{r}, s) q^{+}(\mathbf{r}, s), \tag{5}$$

where $q(\mathbf{r}, s)$ and $q^{+}(\mathbf{r}, s)$ are the forward and backward propagators, which represent the probabilities of finding a segment s at position $\mathbf{r}$. They are solved through the modified diffusion equations

$$\frac{\partial}{\partial s} q(s, \mathbf{r}) = \nabla^2 q(s, \mathbf{r}) - w_i q(s, \mathbf{r}), \tag{6}$$

$$\frac{\partial}{\partial s} q^{+}(s, \mathbf{r}) = -\nabla^2 q^{+}(s, \mathbf{r}) + w_i q^{+}(s, \mathbf{r}). \tag{7}$$

The w_i in Eq. (1) is the self-consistent field potential of component i. In Eqs. (6) and (7), this quantity is w_A, if $0 < s < f \cdot f_A$, and w_B, if $f \cdot f_A < s < f$. The initial condition on the forward propagator, $q(s, \mathbf{r})$, is $q(0, \mathbf{r}) = 1$ for both the ABP and APB systems. The initial condition on the backward propagator, $q^{+}(s, \mathbf{r})$, is $q^{+}(f, \mathbf{r}) = \int d\mathbf{n} \exp(-w_p(\mathbf{r} + R_P\mathbf{n}))$ for the ABP system, while it is $q^{+}(f, \mathbf{r}) = 1$ for the APB system. The symbol $\mathbf{n}$ denotes the unit vector, which specifies the direction from the surface of a particle to the adjacent segment of the copolymer chain. The forward and backward propagators are then determined using Eqs. (6) and (7).

Minimizing the free energy of Eq. (1) with respect to the system variables $w_A(\mathbf{r})$, $w_B(\mathbf{r})$, $w_P(\mathbf{r})$, $\phi_A(\mathbf{r})$, $\phi_B(\mathbf{r})$, $\rho_P(\mathbf{r})$, and $\xi(\mathbf{r})$ yields the mean-field equations

$$\phi_A(\mathbf{r}) = \frac{V}{Q} \int_0^{f \cdot f_A} ds\, q(s, \mathbf{r}) q^{+}(s, \mathbf{r}), \tag{8}$$

$$\phi_B(\mathbf{r}) = \frac{V}{Q} \int_{f \cdot f_A}^{f} ds\, q(s, \mathbf{r}) q^{+}(s, \mathbf{r}), \tag{9}$$

$$\rho_P(\mathbf{r}) = \frac{V}{Q} \exp(-w_P(\mathbf{r})) \int d\mathbf{n}\, q(f, \mathbf{r} + \mathbf{n}R_P), \quad \text{(ABP)} \tag{10}$$

$$\rho_P(\mathbf{r}) = \frac{V}{Q} \exp(-w_P(\mathbf{r})) \times \int d\mathbf{n}\, q(f \cdot f_A, \mathbf{r} + \mathbf{n}R_P) \times q^{+}(f \cdot (1 - f_A), \mathbf{r} + \mathbf{n}R_P), \quad \text{(APB)} \tag{11}$$

$$w_A(\mathbf{r}) = \chi_{AB} N \phi_B(\mathbf{r}) + \chi_{AP} N \phi_P(\mathbf{r}) + \xi(\mathbf{r}), \tag{12}$$

$$w_B(\mathbf{r}) = \chi_{AB} N \phi_A(\mathbf{r}) + \chi_{BP} N \phi_P(\mathbf{r}) + \xi(\mathbf{r}), \tag{13}$$

$$\begin{aligned} w_P(\mathbf{r}) = {} & \psi_{HS}(\bar{\phi}_p(\mathbf{r})) \\ & + \frac{1 - f}{V_{2R}} \int_{|r'| < 2R_P} d\mathbf{r}' \rho_P(\mathbf{r}' + \mathbf{r}) \psi'(\bar{\phi}_P(\mathbf{r} + \mathbf{r}')) \\ & + \frac{1 - f}{V_R} \int_{|r'| < R_P} d\mathbf{r}' [\chi_{AP} N \phi_A(\mathbf{r}' + \mathbf{r}) \\ & + \chi_{BP} N \phi_B(\mathbf{r}' + \mathbf{r}) + \xi(\mathbf{r}' + \mathbf{r})], \end{aligned} \tag{14}$$

$$\phi_A(\mathbf{r}) + \phi_B(\mathbf{r}) + \phi_P(\mathbf{r}) = 1, \tag{15}$$

where

$$\psi'_{HS}(\bar{\phi}_P) = \frac{d\psi_{HS}}{d\bar{\phi}_P(\mathbf{r})}. \tag{16}$$

We used the Alternating Direction Implicit Method with periodic boundary conditions in three dimensions to solve the SCFT/DFT equations.[46–48] The calculation results were used for the combinatorial screening of new mesophases in BCP-NP systems. A simulation began with setting the initial values of $\phi_A(\mathbf{r})$ and $\phi_B(\mathbf{r})$ according to the Gaussian distribution, while the initial value for the particle center distribution function, $\rho_P(\mathbf{r})$, was uniform and the initial Lagrange multiplier $\xi(\mathbf{r})$ was set to the null value. Next, calculations were performed of the particle volume fraction $\phi_P(\mathbf{r})$ via Eq. (2), the weighted non-local volume fraction $\bar{\phi}_P(\mathbf{r})$ from Eq. (3), and the self-consistent field potential fields $w_A(\mathbf{r})$, $w_B(\mathbf{r})$, $w_P(\mathbf{r})$ from Eqs. (12)–(14). The propagators $q(s, \mathbf{r})$ and $q^{+}(s, \mathbf{r})$ could then be determined, which were used to calculate the copolymer chain partition function Q from Eq. (5). The next step evaluated the local block volume fractions $\phi_A(\mathbf{r})$, $\phi_B(\mathbf{r})$ using Eqs. (8) and (9), while the particle volume fraction $\phi_P(\mathbf{r})$ and the weighted non-local volume fraction $\bar{\phi}_P(\mathbf{r})$ were determined using Eqs. (2) and (3) after evaluating $\rho_P(\mathbf{r})$ using Eqs. (10) and (11). The surface integrals in Eqs. (10) and (11) were approximated with sufficient accuracy using the mean-value theorem, $\int f(\mathbf{n}) d\mathbf{n} = \bar{f} \cdot S$, where S is the area of the surface of integration and $\bar{f}$ is the mean value of $f(\mathbf{n})$ over the surface. The Lagrange multiplier $\xi(\mathbf{r})$ was calculated according to Eqs. (12) and (13) under the incompressibility constraint of Eq. (15). Finally, the potential fields $w_A(\mathbf{r})$, $w_B(\mathbf{r})$, $w_P(\mathbf{r})$, and $\xi(\mathbf{r})$ were updated using a simple mixing method and the procedure was iterated until convergence was achieved.[29,48] The calculations were carried out until the self-consistent field potential differences between two consecutive iterations were smaller than 10^{-5}, and the incompressibility condition was satisfied.[32,35,41]

The calculation box size must be determined in correspondence with the natural periodic length of the system morphology, especially in the transition regions between lamellar, spherical, and cylindrical structures. We performed verifications typically using 12 different box sizes varying from about 4.6 R_g to 6.9 R_g (from $32 \times 32 \times 32$ to $48 \times 48 \times 48$ cell numbers) with cell cubes of dimension 0.144 R_g with 200 segments of a Gaussian chain. We used different initial conditions to decide which morphology was the most stable by comparing their free energies.[28] We varied f_A and $\chi_{AB}N$ systematically to construct phase diagrams for the target systems

in Table I in order to determine the most promising morphologies for nanofiltration applications and the strategies (i.e., parameter mappings) required to generate them. Each phase diagram presented below consists of results of 3D simulations covering 91 distinct points in a representative range of parameter space, (f_A, $\chi_{AB}N$), optimizing box size as necessary.

III. RESULTS AND DISCUSSION

In each of the five target systems, the cylinder, lamellar, and spherical morphologies were the most stable ordered structures formed during the self-assembly process. The particles were generally distributed unequally in the two block copolymer domains, and often agglomerated into distinct particle-dense regions of the self-assembled structures, as described in Sec. III C.

A. Phase diagram of end-tethered particle systems

We examined three separate cases of end-tethered particles. In each case, the particle was tethered to the free end of the B-block of the copolymer. The three systems studied correspond to cases where the particle is neutral to both blocks of the copolymer (ABP-N), where it disfavors the A-block but favors the B-block (ABP-AP), and vice versa (ABP-BP). We will discuss each of these three cases in Secs. III A 1 and III A 2.

1. The neutral particle system (ABP-N)

The ABP-N system of end-tethered nanoparticles was first studied using 2-dimensional SCFT/DFT simulations by Zhu *et al.*,[35] for which $\chi_{AP}N = \chi_{BP}N = 0$. We performed 3D simulations of the same system at $R_P/R_g = 0.33$ over similar ranges of $\chi_{AB}N$ ($\in$[11,28]) and f_A ($\in$[0.2,0.8]) as assumed by Zhu *et al.* Figure 1 presents the phase diagram of these 3D

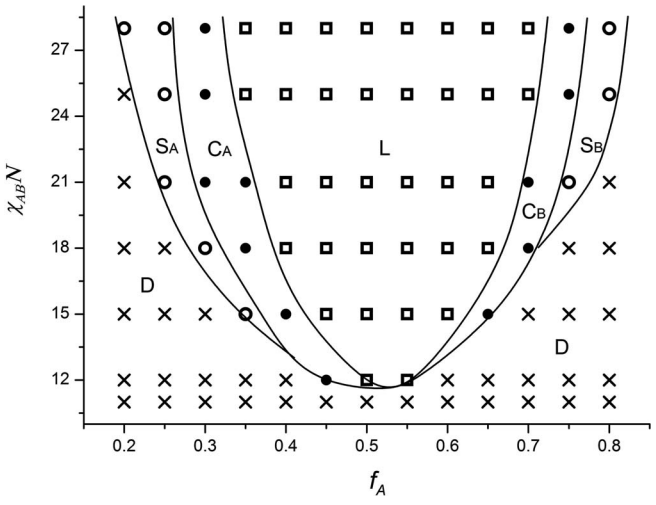

FIG. 1. Morphological diagram of the ABP-N system, as defined in Table I. The different morphological regions are denoted as lamellae (L), hexagonally packed cylinders formed by the A block (C_A), cylinders formed by the B block (C_B), nanospheres formed by the A block (S_A), nanospheres formed by the B block (S_B), and disordered phases (D).

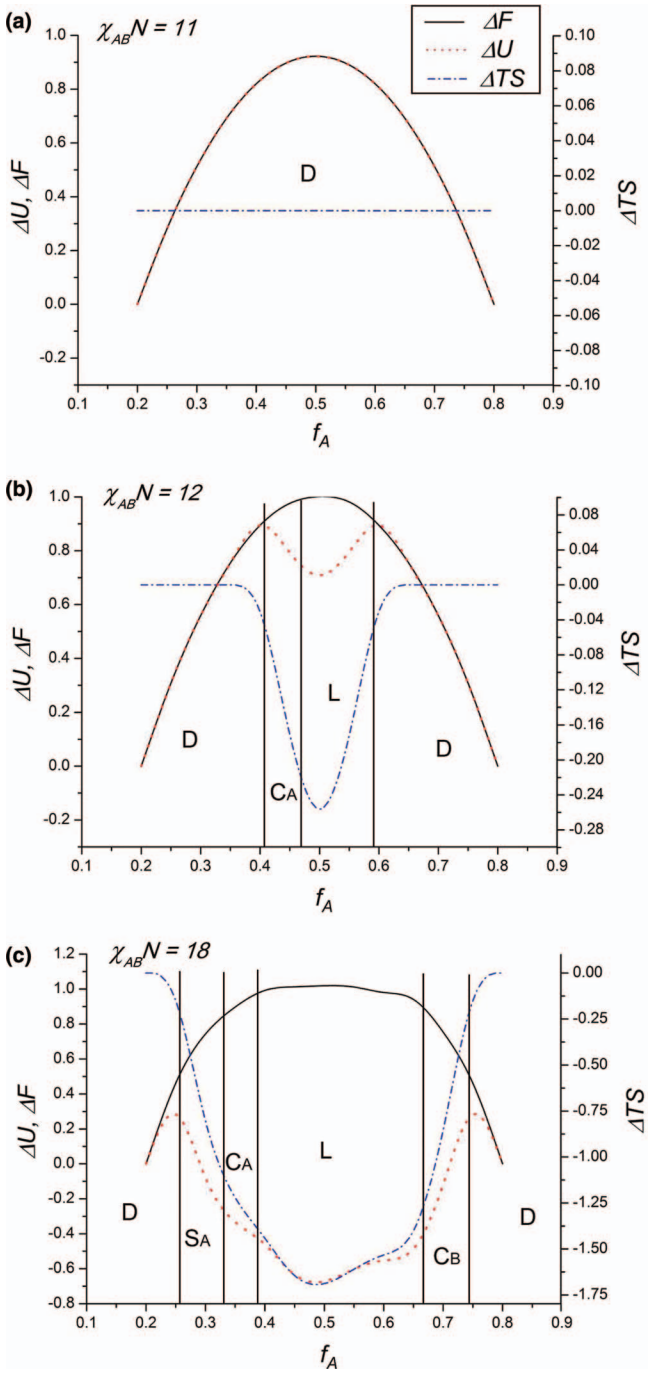

FIG. 2. Energetic and entropic contributions to the free energy at various values of $\chi_{AB}N$, as noted in the legends. ΔU and $\Delta(TS)$ are calculated relative to their values at $f_A = 0.2$ at the respective value of $\chi_{AB}N$. The vertical lines denote the approximate phase boundaries of the various morphologies.

simulations, which is similar to the phase diagram of stable, 2D morphologies of Zhu *et al.*; however, the phase diagram for our system is shifted to lower values of $\chi_{AB}N$ than that of Zhu *et al.* for the appearance of the ordered regions (cf. Fig. 1, where $\chi_{AB}N \approx 12$ at the ordered-phase critical point, with Fig. 2 of Zhu *et al.*, where $\chi_{AB}N \approx 15$). Presumably, this is due to the 2D confinement effect, i.e., the restriction to 2D increases the miscibility of polymer blends. Therefore, the critical point of their 2D simulation is much higher than a comparable 3D simulation.[49] The particle volume fractions

are also different between our 3D and their 2D simulations: as mentioned above, we chose to use the same value for the ratio $R_P/R_g = 0.33$ as Zhu *et al.*; however, this corresponds to a value of $f_P = 0.098$ in the 2D simulations, whereas it is 0.035 in the 3D simulations. This difference impacts the values of the particle surface and volume integrations appearing in Eqs. (10) and (11), and (14). Therefore, our critical point of the ordered-phase transition is closer to that of the pure diblock copolymer, which is known to occur at a value of $\chi_{AB}N \approx 10$.[40]

As evident from Fig. 1, only disordered morphologies (D) exist for $\chi_{AB}N < 12$. For higher values of this parameter, one also finds five distinct ordered morphologies depending on the volume fraction of the A-block. At relatively low values of f_A, there exists a morphology composed of A-rich cylinders (C_A) that are hexagonally packed within the B-dominated matrix region. Conversely, at relatively high values of f_A, the hexagonal cylinders are rich in the B-block of the copolymer (C_B), surrounded by an A-rich matrix phase. Typical values of the local volume block fraction of the dominant cylinder component typically reach 0.95. For intermediate values of f_A, we observe the usual lamellar region (L) where the segregation of the blocks of the copolymer is extreme, with alternating layers typically possessing a local volume fraction of the dominant block in the range of [0.9, 0.95]. Two spherical morphologies, S_A and S_B, are formed immediately outside of the C_A and C_B regions, at slightly lower and higher values of f_A, respectively. These morphologies are comprised of nanospheres arranged on body-centered cubic lattices, which are either A-rich or B-rich, depending on the value of f_A.

The spherical morphologies described above were not found in the 2D simulations of Zhu *et al.* at this value of $R_P/R_g = 0.33$—see Fig. 2 of Ref. 35. The reason for this is most likely that the 2D simulations simply were not able to distinguish between the spherical and cylindrical morphologies, and hence the C_A region of the 2D simulations corresponds almost exactly to the combined C_A and S_A regions of the 3D simulations, and likewise for C_B. However, Zhu *et al.* stated that they performed a few sample 3D simulations for this system for R_P/R_g values in the neighborhood of 0.33, but noticed no differences between their 2D and 3D simulation phase diagrams. Therefore, we investigated these regions of our phase diagram very carefully to ascertain the most stable morphology by varying the simulation box size from 4.6 × 4.6 × 4.6 to 6.9 × 6.9 × 6.9 R_g^3 (corresponding to 30 × 30 × 30 to 48 × 48 × 48 cells) and initial conditions (covering metastable morphologies of disordered, cylindrical, and spherical states formed from previously converged solutions). Zhu *et al.* stated that they examined box sizes of 48 × 48 × 48, whereas most of our minimum free energy states were determined with boxes sizes in the neighborhood of 33 × 33 × 33 or 42 × 42 × 42. For a box size of 48 × 48 × 48, we found free energy values significantly higher than those for smaller box sizes, and morphologies that were either perforated lamellar[40,41] or gyroidal[40,42,43] for various box sizes, depending on the state point. The accuracy of the particle surface integration in our model is limited by the lattice size, which might cause the free energy comparisons between the various morphologies at specific state points in these narrow regions of phase space to contain numerical approximation errors; however, the particular morphology we report at each state point corresponds to the one with the absolute lowest value of the free energy as calculated in our simulations. Regardless of any possible approximation error, we believe that these more complex morphologies, if occurring at all, only exist in such narrow regions of state space (at least at the particle size examined herein) as to be practically inaccessible. Specifically, the difference between two simulation state points is $0.05f_A$ at the same value of $\chi_{AB}N$, whereas the region where the gyroidal morphology is present is known to be quite narrow (<0.05), and the cylinder or lamellar regions are also known to overlap partially the gyroidal region (which is only metastable in these overlapping regimes).[48] These reasons make it is difficult to determine the exact gyroidal region of global stability in this method, assuming that it exists. Note that at higher values of R_P/R_g (0.45), Zhu *et al.* did observe spherical morphologies of the sort noted above. (For the value of $R_P/R_g = 0.45$, the corresponding value of f_P is 0.0835.)

It is instructive to examine the behavior of the internal energy and entropy of the stable morphologies within the various regions of the phase diagram—see Fig. 2. For this purpose, the free energy of Eq. (1) is split into components arising from energetic effects (the first three terms within the integral), which we assign the symbol U, and entropic effects (all other terms), which we define as S, according to the standard Legendre transformation, $F = U - TS$. Each of these quantities is rendered dimensionless in the same way as the free energy of Eq. (1), with U relative to $N_C k_B T$ and S relative to $N_C k_B$. At $\chi_{AB}N = 11$, the system is always in the disordered regime regardless of the value of f_A. The energetic contribution to the free energy displays a maximum at roughly $f_A \approx 0.5$. (This maximum occurs slightly less than $f_A = 0.5$ because of the non-zero value of the particle volume fraction, $f_P = 0.035$.) The energetic contribution for the ABP-N system varies as the integral of $\chi_{AB}N\phi_A\phi_B \approx \chi_{AB}N\phi_A(1 - \phi_A)$ since $\phi_P \ll 1$, so in a disordered state, where the local concentration of each block is roughly proportional to its relative fractional chain length, the maximum of ΔU in the vicinity of $f_A \approx 0.5$ is expected. The entropic contribution remains null, independent of the value of f_A, which is a consequence of the assumption of statistical equivalence of the A and B segments (sometimes referred to as "conformational symmetry"). Since the A and B segments are indistinguishable from each other in the model, as long as the overall chain length remains the same there is no configurational entropic effect associated with varying the relative lengths of the blocks. With $\Delta S = 0$, the free energy change with increasing f_A is equivalent to ΔU. Although the change in entropy (relative to its value at $f_A = 0.2$) is $\Delta S = 0$ regardless of f_A, its absolute value is not zero, and configurational entropy is the dominant driving force in maintaining the disordered state of the system in spite of the non-zero value of $\chi_{AB}N = 11$.

When the interaction parameter is increased to $\chi_{AB}N = 12$, as in Fig. 2(b), ordered phases develop in the vicinity of $f_A \approx 0.5$—see Fig. 1. The increased interaction energy, U, has grown to a magnitude to where it can compete with the randomizing entropic potential, S. At small and large values of f_A, the entropy can still overcome the energetics of the

repulsive forces between the A and B segments since the number of interactions is fewer than when the blocks have an equal number of segments. In these regions, the phase is disordered and the energy and entropy display the same qualitative behavior as for the case of $\chi_{AB}N = 11$. For $f_A \approx 0.5$; however, the energy can be reduced by phase segregating the A and B segments, as mandated by the parabolic expression $\chi_{AB}N\phi_A(1 - \phi_A)$, which nears global minima as $\phi_A \to 0, 1$. This segregation results in a large decrease in the configurational entropy due to packing frustration as the chains adopt unnatural configurations, which drives up the free energy. The chain configurations are compressed and packed within the minor phase domains, whereas the chains comprising the matrix phase are stretched in accordance with the constant density assumption. Nevertheless, this randomizing driving force is not severe enough to overcome the energetic decrease, leading to a stable ordered phase. Phases of cylinders or lamellae are formed, depending on the relative block lengths (i.e., the value of f_A), with the junctures and particles primarily located at the interfaces. The surface area of these interfaces is determined by a delicate balance between the entropic packing frustration within the structure and the necessity of minimizing the contact area between the A and B segments. The exact morphology (cylinders, lamellae, or, at higher χ_{AB}, spheres) that appears is determined largely by this balance between the packing volume of the structure and its interfacial surface area. As the relative lengths of the blocks changes (varying f_A), this balance can change drastically, hence requiring more numerous but smaller domains (higher surface area to volume ratio), vice versa, or, in the most drastic cases, a change in the morphology of the system to accommodate it.

When the interaction parameter is increased to $\chi_{AB}N = 18$, there are five distinct morphological regimes: D, S_A, C_A, L, C_B, and D, moving from left to right in Fig. 2(c). At this value of $\chi_{AB}N$, the energetic contribution to the free energy is comparable to that of the entropy, and more morphologies arise to accommodate the required balance between interfacial surface area and packing volume. Furthermore, these structures appear for smaller minority chain lengths (i.e., smaller and larger values of f_A) than for the case of $\chi_{AB}N = 12$ since the relative contribution of the entropy to the free energy has decreased.

2. Interacting particle systems (ABP-AP and ABP-BP)

Zhu *et al.*[35] also examined a 2-dimensional system wherein particles tethered to the end of one of the blocks were disfavored equally by both of the blocks of the copolymer. Here we study the case where the end-tethered particle favors the B block, to which it is attached, while disfavoring the A block (ABP-AP) and the inverse case (ABP-BP), as displayed in Table I. We retained the particle radius at $R_P/R_g = 0.33$.

In the case of the ABP-AP system, we set the particle-block interaction parameters at values of $\chi_{AP}N = 30$ and $\chi_{BP}N = -30$, such that the particle has an affinity to the B block to which it is tethered and a revulsion to the A block. Since the particles are attached to the B blocks, we expect that the phase diagram for this system will qualitatively resemble

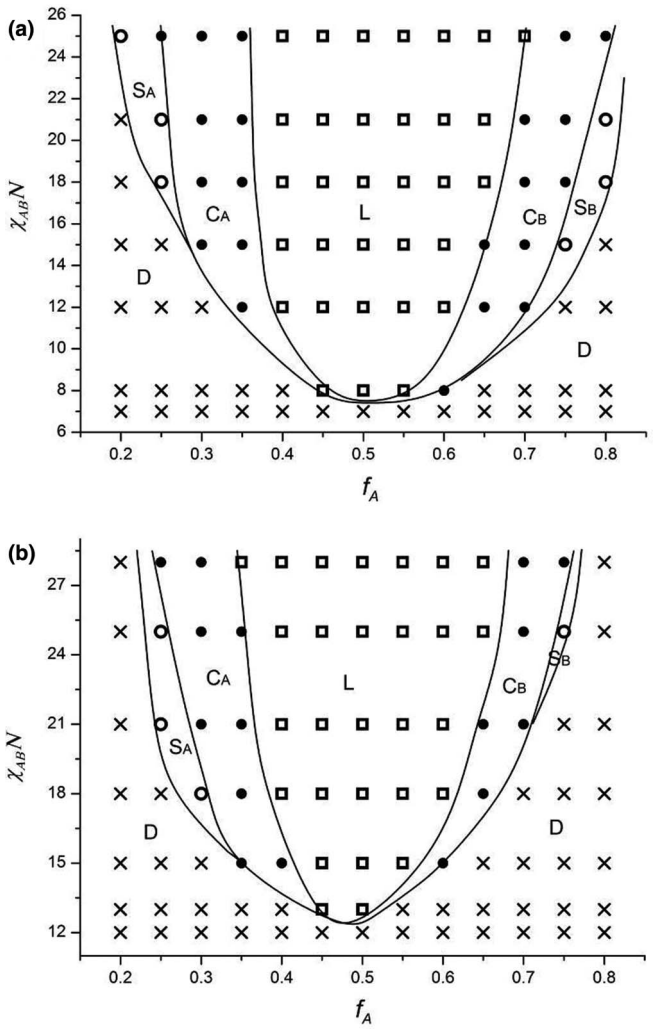

FIG. 3. (a) Morphological phase diagram of the ABP-AP system with favorable BP interactions and unfavorable AP interactions. (b) Phase diagram of the ABP-BP system with favorable AP interactions and unfavorable BP interactions.

that of the ABP-N system, but drive the particle distribution even more prominently into the domains of the self-assembled structures that are dominated by the B block. Consequently, one could possibly tailor in a specific volume fraction of particles within the B-rich regions of the morphologies by fine-tuning the affinity of the particles to the B block of the copolymer, as discussed in Sec. III C.

The phase diagram for the ABP-AP system is presented in Fig 3(a). For $\chi_{AB}N < 8$, only the disordered phase was stable as the order-inducing energetic contribution of the repulsive A-B block interactions was not sufficient to overcome the randomizing entropic contributions to the free energy. An evident change from the ABP-N system of Fig. 1 is that the ordered-phase critical point in the ABP-AP system has been shifted downward on the $\chi_{AB}N$-axis relative to that of the ABP-N copolymer. Because the $\chi_{AP}N$ and $\chi_{BP}N$ parameters are no longer zero, two additional terms in Eq. (1) are contributing to the internal energy of the system. Although the terms $\chi_{iP}N\phi_i\phi_P$ can significantly impact the free energy in localized domains, which are relatively rich in particles, they do not contribute substantially to the overall free energy of the

system since $f_P \ll 1$. Nevertheless, the primary driver of this downward shift is the affinity of the B segments for the particles, which induces the B segments to cluster and compress around the particles, thereby reducing the number density of particles and B segments directly exposed to the A blocks. This not only results in a lower overall internal energy contribution to the total free energy, but also relieves some of the entropic packing stress, thus allowing ordered phase segregation at lower values of $\chi_{AB}N$ than in the ABP-N system. Another key change evident in Fig. 3(a) from the ABP-N phase diagram of Fig. 1 is that the C_A and C_B regions have widened whereas the lamellar region has shrunk, which is likely due to the lowering of the internal energy by the negative BP interactions (recall that $\chi_{BP}N\phi_B\phi_P$ is a negative quantity), thus shifting the ratio of interfacial area to packing volume higher.

The corresponding phase diagram for the ABP-BP system is displayed as Fig. 3(b), where the particle-block interaction parameters were set at $\chi_{AP}N = -30$ and $\chi_{BP}N = 30$. In the ABP-BP case, it is evident that the ordered-phase critical point has shifted upward. Now that the particles favor the A segments, rather than the B blocks to which they are tethered, a huge entropic penalty must be overcome to form an ordered phase since the particles preferentially tend to concentrate at the interfaces where they can be near to the A segments, thus forcing the B blocks to assume loop and hairpin-like configurations, or to stretch across the dimensions of the domain. Consequently, the overall contribution of the internal energy to the free energy must be significantly larger than in the neutral particle (ABP-N) case to overcome the large reduction in short-range configurational entropy of the B blocks—refer to Fig. 2, which is qualitatively similar to the present case. The morphological phase diagram of Fig. 3(b) resembles more that of the neutral particle case of ABP-N (Fig. 1) than that of the ABP-AP case (Fig. 3(a)). As in the ABP-BP case, the phase diagram exhibits an expanded C_A region, while the C_B region is relatively narrow. The A-rich cylinder morphology of the C_A region is stabilized by the favorable AP interactions.

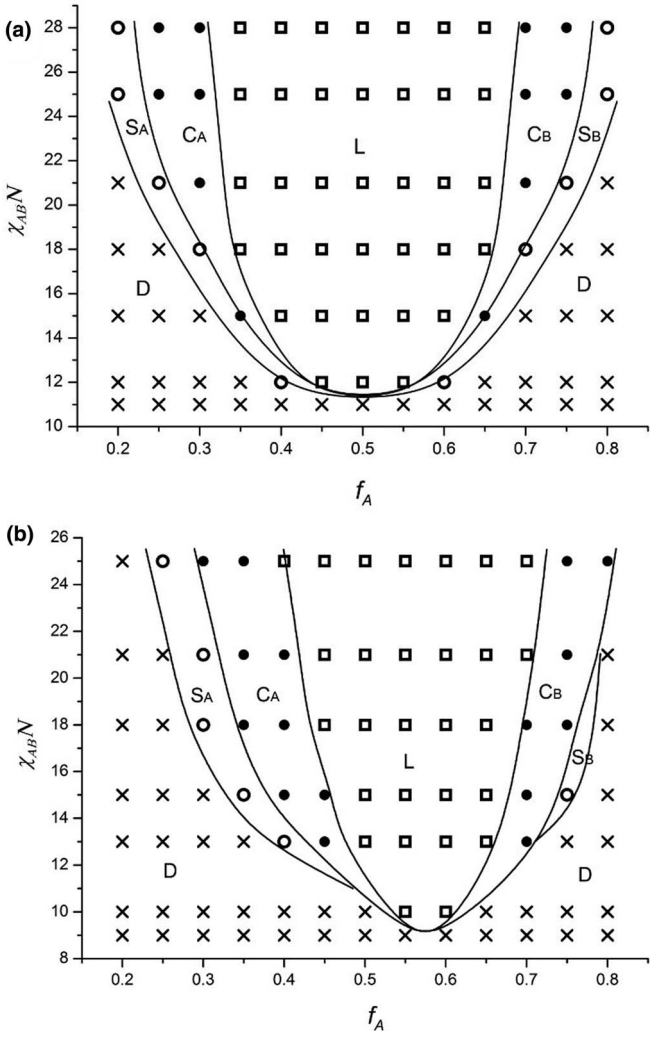

FIG. 4. (a) Morphological phase diagram of the APB-N system in which the particle is tethered between the two blocks and is neutral to both. (b) The phase diagram of the APB-AP system. The particles favor the B blocks and disfavor the A blocks. Due to symmetry, the inverse system, APB-BP, has the same phase diagram when f_A is replaced with f_B.

B. Phase diagram of center-tethered particle systems (APB-N and APB-AP)

We simulated two systems in which the interacting particles were located at the juncture of the diblock copolymer, between the A and B blocks. The first case is that of a particle that is neutral to both blocks (APB-N), and the second where the particle favors the B segments and disfavors the A segments (APB-AP). Note that the second case is statistically equivalent to that in which the particle favors A and disfavors B. Since the particles are tethered between the two copolymer blocks, it seems natural to expect that one might find many interesting morphologies here in which the particles are heavily concentrated at the interfaces between the A-rich and B-rich domains.

The morphological phase diagram of the APB-N systems is presented in Fig. 4(a), where $\chi_{AP}N = \chi_{BP}N = 0$. Because the particle is neutral to both A and B segments, the phase envelope is symmetric about $f_A = 0.5$ since there is no physical difference in this model between A and B blocks, other than through the dimensionless interaction parameters. Again there appear six general types of morphologies, corresponding to disordered domains, A-rich and B-rich cylinders, A-rich and B-rich spheres, and lamellae. The morphological phase diagram for the APB-AP system (center-tethered particle for $\chi_{AP}N = 30$ and $\chi_{BP}N = -30$) is depicted in Fig. 4(b). Compared to the APB-N system, the C_A region of the phase diagram has widened whereas the C_B region has shifted to the right. In all cases, the particles are heavily dispersed within the B-rich domains of the structures, as one would expect given the high degree of affinity between the particles and the B segments—refer to Sec. III C. (Note that this case is equivalent to the APB-BP system with the A and B blocks interchanged.)

C. Particle density distributions

Three types of cylinder morphologies were discovered in the 3D simulations, each with a distinct distribution of particles within the A-block and B-block dominated domains—refer to Fig. 5(a). In reference to Figs. 5(b) and 5(c), and 5(d),

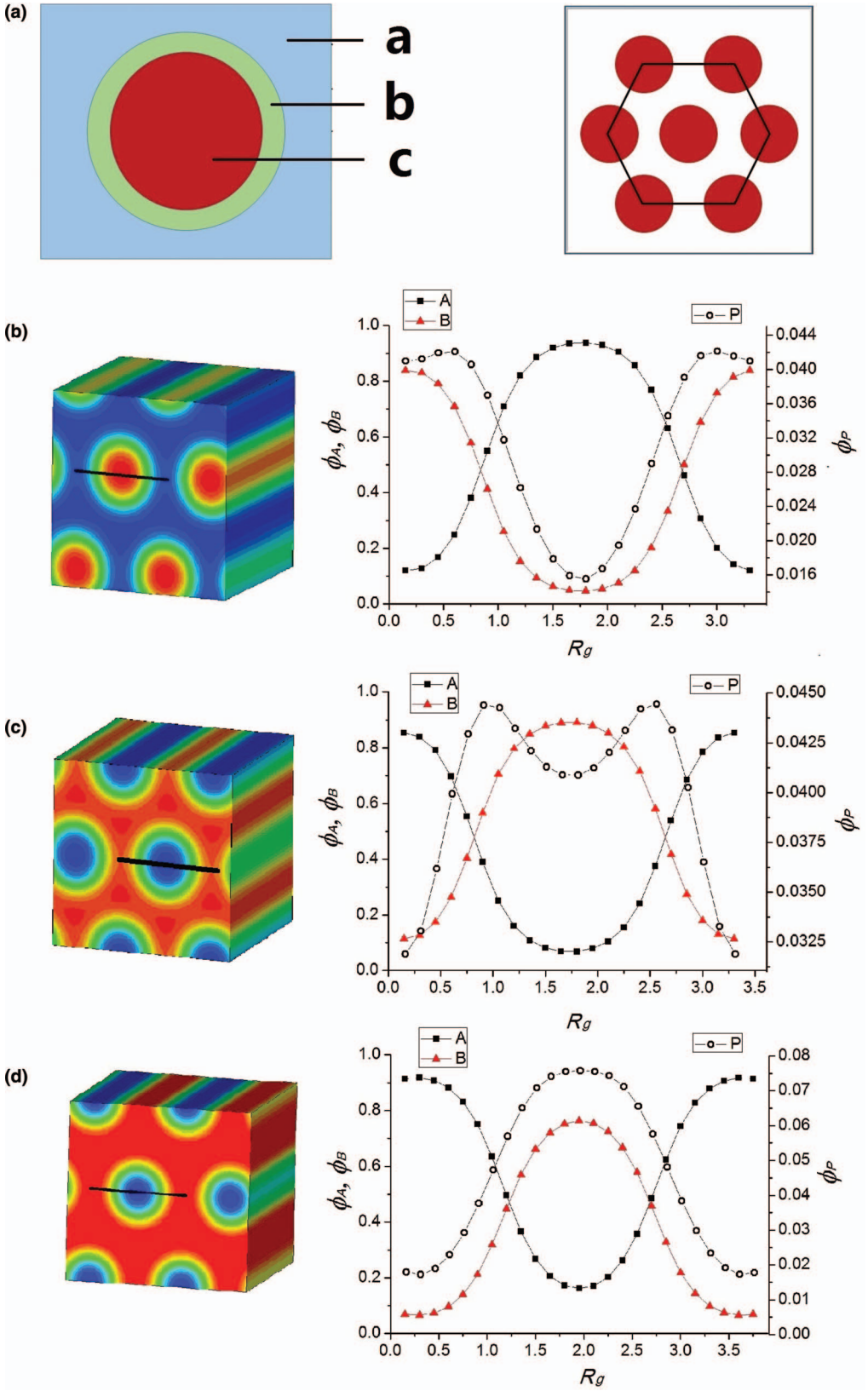

FIG. 5. (a) Schematic diagram of possible particle-rich regions (left) and the cylinder hexagonal packing configuration (right). In the left figure, the symbols denote the following regions of the most stable, ordered cylindrical structure: polymer matrix (a), cylinder interface (b), and cylinder core (c). In the right diagram, the lengths of the black line segments denote the packing dimension. Rows (b), (c), and (d) are the example morphologies (left column) and sample distributions (right column) representing the various regions depicted in (a); (b) particles concentrated within the matrix domain (APB-AP, $f_A = 0.75$, $\chi_{AB}N = 18$); (c) particles concentrated at the interface (ABP-BP, $f_A = 0.65$, $\chi_{AB}N = 21$); and (d) particles concentrated within the cylinder cores (APB-AP, $f_A = 0.35$, $\chi_{AB}N = 18$). The block and particle volume fractions in the right column are plotted in units of R_g corresponding to the periodic spatial location along the black line in the morphological images on the left.

TABLE II. Typical values of cylinder diameters and packing dimensions. The error associated with these values is $\pm 0.14\ R_g$, which is due to the discretization of the simulation grid.

System	Diameter (R_g)	Packing dimension (R_g)	$\chi_{AB}N$	f_A
ABP-N	[2.0, 2.2]	[4.1, 4.6]	21	[0.3, 0.35]
	[2.0, 2.5]	[4.1, 5.0]	[21, 25]	0.3
ABP-AP	[2.1, 2.5]	[4.4, 4.7]	25	[0.25, 0.35]
	[1.8, 2.5]	[3.0, 4.7]	[12, 25]	0.35
ABP-BP	[1.3, 1.8]	[3.0, 4.1]	25	[0.3, 0.35]
	[1.5, 1.8]	[3.0, 4.1]	[15, 25]	0.35
APB-N	[1.6, 2.1]	[3.1, 3.4]	25	[0.25, 0.3]
	[1.4, 2.1]	[3.0, 3.4]	[21, 25]	0.3
APB-AP	[2.4, 3.0]	[4.8, 5.0]	25	[0.3, 0.35]
	[2.0, 3.0]	[4.4, 5.0]	[18, 25]	0.35

these three morphologies are as follows: (a) particle-rich matrix domains surrounding hexagonally packed, particle-lean cylinder cores; (b) particle-rich interfaces between the cylinders of one block and the matrix formed by the other; and (c) particle-concentrated cylinder cores surrounded by a particle-depleted matrix phase with a dilute layer of screening particles at the interface. Three important factors acted concertedly to affect particle location during the self-assembly process, as well as the cylinder diameter and the length scale of the hexagonal array: (1) the location of the tethering point of the particle to the copolymer chain, (2) the particle-block interaction parameters and the block-block interaction parameter ($\chi_{ij}N$), and (3) the A-block volume fraction (f_A). The effects of these quantities on the phase diagrams of Secs. III A and III B of the self-assembled structures will be described in the following paragraphs, focusing primarily on the cylinder morphologies rather than those forming lamellae or spheres, as being of greater interest to nanofiltration applications.

With reference to Table II, the values of the cylinder diameters in the C_A and C_B regions are determined based on the intersection of the ϕ_A and ϕ_B curves in Figs. 5(b) and 5(c), and 5(d), and the packing dimensions are defined as the distance between neighboring cylinder centers. These values are critically important for steric exclusion in nanofiltration membranes. Typical values of the cylinder diameter and packing dimension for different values of f_A and $\chi_{ij}N$ are displayed in Table II. The results are as one would intuitively expect: as $\chi_{AB}N$ is increased at fixed f_A, the diameter of the cylinders and the packing dimension increase. This trend occurs because the cylinder surfaces require less curvature (i.e., less surface area relative to volume) since the associated decrease in internal energy is mitigated by the increased energetics of the mismatch between the two copolymer blocks.[40,50] Furthermore, as f_A is increased (when $f_A < 0.5$) at fixed $\chi_{AB}N$, the diameter of the cylinders and the packing dimensions also increase. This is also intuitive since in these C_A morphologies, increasing the length of the A block increases the potential for packing frustration, which balances the energetics of the interfacial curvature.

Besides steric exclusion, and equally important factor influencing the rejection ratio of nanofiltration membranes is the charge (Donnan) exclusion. To proceed, it is necessary to set quantitative criteria as to acceptable design specifications, i.e., concentration levels of particles at the interface, etc. This is, of course, rather arbitrary without a specific application in mind, so we set rather strict criteria and screen parameter space to identify cylindrical morphologies that possess cores with a local volume fraction of the major component of at least 0.80 while that of the minority phase is less than 0.10, as well as interfaces with local particle volume fractions that are at least 75% greater than the overall particle concentration of $f_P = 0.035$, i.e., $\phi_P \approx 0.06$.

Table III displays information about each of the cylindrical morphologies observed in the simulations: the domain with the greatest concentration of particles, the average values of ϕ_P at the interfaces, and whether or not it is possible for the specific morphology to meet the NF membrane design criteria, as stated above. The particles in the ABP-N system are primarily uniformly distributed within the B-rich domains for all ordered morphologies occurring within the investigated region of parameter space, (f_A, $\chi_{AB}N$), which confirms the results of Zhu *et al.* at this value of $R_P/R_g = 0.33$. This is intuitively expected, since the particles do not disfavor either block, and thus effectively act as an additional non-interacting B segment at the end of B block. Consequently, there is no energetic driving force to preferentially distribute the

TABLE III. The particle-rich domains for different cylindrical morphologies in BCP-NP systems and particle volume fractions at the interfaces. The matrix, interface, and cylinder core are defined in 5(a). As $\chi_{AB}N$ or f_A increases, the particle density also increases (but generally less than 0.01 in absolute value).

System	Morphology region	Particle-rich domain	Typical value of particle density at the interface	Candidate for NF?
ABP-N	C_A	Matrix	~0.035	
	C_B	Cylinder core	~0.065	Yes
ABP-AP	C_A	Matrix	~0.040	
	C_B	Cylinder core	~0.075	Yes
ABP-BP	C_A	Interface	~0.045	
	C_B	Interface	~0.050	
APB-N	C_A	Interface	~0.055	Yes, if $\chi_{AB}N \geq 28$
	C_B	Interface	~0.055	Yes, if $\chi_{AB}N \geq 28$
APB-AP	C_A	Matrix	~0.050	Yes, if $\chi_{AB}N > 21$
	C_B	Interface	~0.070	Yes

particles non-uniformly within the A or B blocks, and the particle distribution is then naturally concentrated within the B-rich domains since it is tethered to the end of this block. In the C_B region of parameter space, the particle volume fraction at the interface is approximately 0.065, and the concentrations of the A and B blocks within the cylinder cores and matrix, respectively, are approximately 0.85; hence this region of the morphological phase diagram meets the criteria for application to nanofiltration membranes.

For the ABP-AP system, however, this is more than simply an entropic effect induced by the attachment to the B block, but is also due to the high affinity of the B segments toward the particles, which provides them with a strong energetic motivation to cluster around the particles, in addition to the incompatibility of the particles with the A segments. As in the ABP-N system, an acceptable particle concentration (approximately 0.075) can be achieved at the interfaces in the C_B region of parameter space. Another positive improvement over the ABP-N system is that the cylinder domain regions (C_A and C_B) of the phase diagram are much wider than the previous case, allowing more flexibility in the tuning of design parameters.

In the case of the ABP-BP system, where the particles disfavor the B segments and favor the A segments, the cylinders are very diffuse, with wide interfaces. Although the particle distribution exhibits peaks in the relatively large interfacial regions, the overall magnitude of ϕ_P does not meet the stated design criterion of 0.06. Furthermore, the concentration of the respective blocks within the matrix or cylinder cores is very low, approximately 0.7.

In the APB-N system, the particles act merely as a screen to shield the A and B segments from each other. Consequently, the maximum concentration of particles occurs at the interfaces, where the particles act to screen the A and B segments from each other. Nevertheless, since the particles are neutral to both types of segments, there is a significant concentration of particles that remain in the cylinder cores and the matrix phase, thus reducing the concentration at the interface to a value below the stated design criterion. However, increasing the degree of mismatch between the A and B segments can drive more particles to the interface, where they reduce the system energy by screening the A and B segments from each other; hence an acceptable value of ϕ_P can actually be achieved if $\chi_{AB}N$ is high enough.

The APB-AP system, in which particles disfavor the A segments and favor the B segments, provides a very wide range of possibilities for NF membrane applications. When the length of the A block is relatively small (the C_A region), A segments are predominantly located within the cylinder cores, with a high concentration of particles at the interface screening the B blocks; however, these particles are only located there because of their location along the chain (i.e., tethered between the A and B blocks) simply because from the viewpoint of the A segments, the particles are energetically more unfavorable than the B segments at low values of $\chi_{AB}N$. Nevertheless, the highest particle concentration is within the matrix domain since the particles are attractive to the B segments, which thus tend to surround them. As $\chi_{AB}N$ is increased, the energetic mismatch between the A and B segments increases in magnitude relative to the mismatch between the A segments and particles ($\chi_{AP}N = 30$), and hence the A blocks ultimately view the particles as simply additional B segments. Hence there is a decreasing energetic tendency for the A blocks to push the particles away from the interface and into the matrix phase. At the same time, there is a lower driving force for the B blocks to pull the particles into the matrix phase since the B segments increasingly want to avoid the interfaces where they come into close proximity with the A segments. Hence, as $\chi_{AB}N$ is increased, the natural location of the center-tethered particles concentrates them at the interface, and it indeed becomes possible to meet the stated design criteria. When the A blocks are relatively long (the C_B region), the natural tendency of the A segments to repulse the particles pushes them toward regions of high interfacial curvature, forcing the B segments into highly compacted cylinder cores. This effect intensifies as $\chi_{AB}N$ is elevated, since the degree of mismatch between the A and B segments increases relative to the A-P and B-P interactions. Consequently, the particles are increasingly located at the interfaces, given their tethering location between the two blocks. In both the C_A and C_B regions, the cylinder cores and surrounding matrix are almost entirely free of the opposite segments at high values of $\chi_{AB}N$, i.e., ϕ_A and ϕ_B of approximately 0.95 in their respective domains. Note that the APB-BP morphological phase diagram is simply the mirror image of the APB-AP diagram, so the stated conclusions also apply to the APB-BP system.

In summary, the most reliable way to produce copolymer thin films with cylinders of highly concentrated particles at the interface is to have particles that possess a high affinity for the B segments while strongly disfavoring the A segments. In this case, a moderately sized domain of the phase diagram, the C_B region, is accessible to this particular morphology. Careful tuning of the relevant interaction parameters between the blocks and the particles might therefore provide a pathway to tailoring of both steric and charge screening in nanoporous copolymer membranes once the cylinder-forming block of the copolymer has been thermally or chemically degraded.

D. Critical point of the phase diagrams

It is interesting to examine the effect that particle affinity has upon the ordered-phase segregation in the ABP and APB systems. The critical point of the ordered-phase envelope is displayed as a function of different pairs of $\chi_{AP}N$ and $\chi_{BP}N$ at $f_A \approx 0.5$ in Fig 6. For the ABP system (Fig. 6(a)), the left most datum point corresponds to the ABP-BP system studied above, and the right most to the ABP-AP system, with the ABP-N system at the center of the profile. When the particles are highly repulsive to the B segments and highly attractive to the A segments, the critical point remains constant at a value of $\chi_{AB}N \approx 13$. In this regime, the entropically unfavorable configurations caused by the particle attraction to the A segments dominate the overall free energy, as described above. Because of this, morphologies with the desired concentration of particles at the interface of the cylinder domains cannot be achieved. As the particle interaction strength decreases, the energetic effects begin to counteract the effect of the

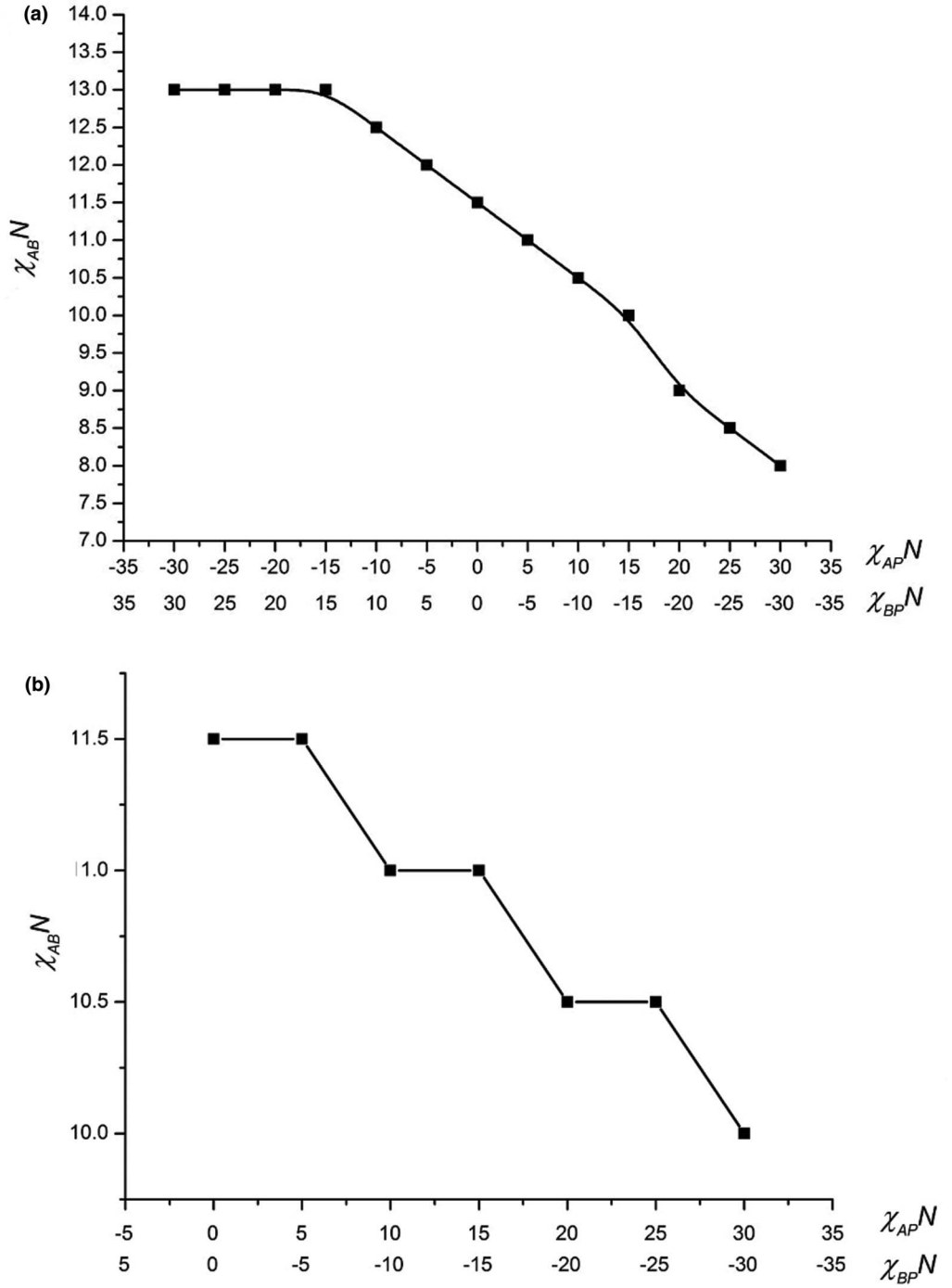

FIG. 6. Values of $\chi_{AB}N$ of the ordered-phase critical points for diblock copolymers as functions of the particle/block interaction parameters: (a) end-tethered particles and (b) center-tethered particles. Note that the data profile in (b) should be symmetric around the point $\chi_{AP}N = \chi_{BP}N = 0$ due to the symmetry of the APB systems.

configurational entropy until the particles are completely neutral in the ABP-N system. Here the particles tend to agglomerate at the interface to screen the A and B segments from each other, producing a counterintuitive high concentration of particles between the cylinder cores and matrix phase. Moving further to the right in Fig. 6(a), the end-tethered particle primarily acts as an additional B segment, at least from the perspective of the A segments, and so the particle concentration in the A phase, whether in the cylindrical domains (C_A region) or in the matrix phase (C_B region), is exceedingly low; consequently, the particle concentration at the interface and in the B-rich domains is higher than in the neutral particle system. This increasingly high degree of segregation moving to the right in Fig. 6(a) provides the driving force for the decrease in the critical point.

As for the APB system displayed in Fig. 6(b), the qualitative behavior displays the same trend exhibited by the ABP systems, i.e., the minimum decreases with increasing disparity between the two block-particle interaction parameters moving to the right from the neutral APB-N system. The

reason for this is the same as above: the increasingly repulsive force between the A segments and the particle drives a higher degree of segregation of the particles at the cylinder interfaces and within the B-rich domains. Consequently, the APB-AP system possesses higher concentrations of particles at the interfaces than the neutral APB-N system, in general, and an increasing value of $\chi_{AP}N$ drives down the ordered-phase critical point and leads to even higher concentrations of particles at the cylinder interfaces. This type of information could be very important for initial screening of particle interaction properties for grafting onto block copolymers designed for specific applications.

IV. CONCLUSIONS

In summary, it was determined that there are a variety of 3-dimensional morphologies that can be produced from the self-assembly of diblock copolymer chains with tethered nanoparticles that possess the desired characteristics for potential application to nanofiltration membranes. Our targeted morphologies were those in which hexagonally packed cylinders, composed primarily of an easily degradable block, were formed within a surrounding non-degradable matrix phase, with a specific concentration of particles at the interface between the two domains. The cylinder diameter, hexagonal packing dimensions, and the distributions of particles at the interfaces could be tuned via varying the interaction parameters of the blocks and particles, as well as using the relative lengths of the copolymer blocks f_A, thus providing an opportunity to tailor the steric and charge screening of potential nanofiltration membranes. As a general guideline, the greatest degree of interfacial particle concentration is achieved when the incompatibility between the two copolymer blocks is fairly high, but this may lead to cylinders of larger diameter with more diffuse interfaces for end-tethered particle systems. Hence both steric and charge exclusion would decrease simultaneously. However, the cylinder size could be more effectively controlled, especially if smaller diameter cylinders are desired with sharp interfaces, by choosing particles that are very incompatible with one of the copolymer blocks. Nevertheless, the number of competing phenomena, which contribute to the overall balance of entropy and energetic effects that constitute the overall free energy is so delicate that identifying general trends is very difficult.

The pore size is critical for steric exclusion in nanofiltration applications, as is their number density, which is closely related to the packing dimension of the hexagonal array. Both of these quantities need to be tuned to ensure that the membrane has a reasonable throughput at low pressures. Consequently, a balance must be struck between the pore diameter, the packing dimension, and the surface charge density of the particles in order to tailor the proper steric and charge exclusion for a particular nanofiltration application, and varying $\chi_{AB}N$ alone will likely not be effective. The most critical parameters dictating pore size are the interaction parameters χ_{ij} and the molecular weight of the copolymer, which can be chosen *a priori* to coarse-tune the approximate pore size of the self-assembled membrane desired. The volume fraction of the A block, f_A, was determined to be only effective at fine-tuning the cylinder diameters and packing dimensions because these quantities vary only slightly with f_A since the C_A and C_B regions are rather narrow.

Given the enormous wealth of unexplored potential membrane materials, it is certainly possible that a judicious design of a diblock copolymer and charged nanoparticle system could ultimately lead to advances in the applicability of nanofiltration membranes. The use of self-consistent field simulations offers another avenue of exploration in this direction for targeting specific design criteria, such as pore size and surface charge density, in nanofiltration membrane production.

ACKNOWLEDGMENTS

We gratefully acknowledge the support of this work by the NSF-funded TN-SCORE program, NSF EPS-1004083, under Thrust 2. Partial funding for this project was also provided by the Sustainable Energy Education and Research Center at the University of Tennessee-Knoxville. Computational resources were provided by the National Science Foundation under Grant No. CBET-0742679 to the PolyHub Virtual Organization.

[1] Y. K. Shim and S. Chellam, "Steric and electrostatic interactions govern nanofiltration of amino acids," Biotechnol. Bioeng. **98**, 451–461 (2007).
[2] A. A. Hussain and A. E. Al-Rawajfeh, "Recent patents of nanofiltration applications in oil processing, desalination, wastewater and food industries," Rec. Pat. Chem. Eng. **2**, 51–66 (2009).
[3] F. G. Donnan and W. E. Garner, "Equilibria across a copper ferrocyanide and an amyl alcohol membrane," J. Chem. Soc. **115**, 1313–1328 (1919).
[4] F. G. Donnan, "The theory of membrane equilibria," Chem. Rev. **1**, 73–90 (1924).
[5] P. Dutournie, L. Limousy, S. Deon, and P. Bourseau, "Unsteady transport of divalent salt through a mineral membrane of ultrafiltration: numerical estimation of physical parameters," Desalination **265**, 184–189 (2011).
[6] P. Dutournie, L. Limousy, N. Zouaoui, H. Mahzoul, and E. Chevereau, "Facilitated transport of monovalent salt mixture through ultrafiltration Na-mordenite membrane: Numerical investigations of electric and dielectric contributions," Desalination **280**, 397–402 (2011).
[7] H. C. Zhu, A. Szymczyk, and B. Balannec, "On the salt rejection properties of nanofiltration polyamide membranes formed by interfacial polymerization," J. Membr. Sci. **379**, 215–223 (2011).
[8] G. M. Geise, L. P. Falcon, B. D. Freeman, and D. R. Paul, "Sodium chloride sorption in sulfonated polymers for membrane applications," J. Membr. Sci. **423–424**, 195–208 (2012).
[9] Q. Zhao, Q. F. F. An, Y. L. Ji, J. W. Qian, and C. J. Gao, "Polyelectrolyte complex membranes for pervaporation, nanofiltration and fuel cell applications," J. Membr. Sci. **379**, 19–45 (2011).
[10] A. Kulkarni, D. Mukherjee, and W. N. Gill, "Flux enhancement by hydrophilization of thin film composite reverse osmosis membranes," J. Membr. Sci. **114**, 39–50 (1996).
[11] G. Decher and J. D. Hong, Buildup of ultrathin "multilayer films by a self-assembly process. 1. Consecutive adsorption of anionic and cationic bipolar amphiphiles on charged surfaces," Makromol. Chem., Macromol. Symp. **46**, 321–327 (1991).
[12] M. Doi, *Introduction to Polymer Physics* (Clarendon Press, Oxford, 2001).
[13] J. Y. Choi, T. Takayama, H. C. Yu, C. M. Chung, and K. Kudo, "Preparation and characterization of nanoporous films derived from alicyclic copolyimides having pendent poly(propyleneglycol) groups," Polymer **53**, 1328–1338 (2012).
[14] T. Hirai, M. Leolukman, C. C. Liu, E. Han, Y. J. Kim, Y. Ishida, T. Hayakawa, M. Kakimoto, P. F. Nealey, and P. Gopalan, "One-step direct-patterning template utilizing self-assembly of POSS-containing block copolymers," Adv. Mater. **21**, 4334 (2009).
[15] E. Reister, and G. H. Fredrickson, "Nanoparticles in a diblock copolymer background: The potential of mean force," Macromolecules **37**, 4718–4730 (2004).

[16]X. G. Ye, B. J. Edwards, and B. Khomami, "Elucidating the formation of block copolymer nanostructures on patterned surfaces: A self-consistent field theory study," Macromolecules **43**, 9594–9597 (2010).
[17]J. J. Schwab and J. D. Lichtenhan, "Polyhedral oligomeric silsesquioxane (POSS)-based polymers," Appl. Organomet. Chem. **12**, 707–713 (1998).
[18]H. Yockell-Lelièvre, J. Desbiens, and A. M. Ritcey, "Two-dimensional self-organization of polystyrene-capped gold nanoparticles," Langmuir **23**, 2843–2850 (2007).
[19]B. Sarkar and P. Alexandridis, "Self-assembled block copolymer-nanoparticle hybrids: Interplay between enthalpy and entropy," Langmuir **28**, 15975–15986 (2012).
[20]E. R. Chan, L. C. Ho, and S. C. Glotzer, "Computer simulations of block copolymer tethered nanoparticle self-assembly," J. Chem. Phys. **125**, 064905 (2006).
[21]J. Huh, V. V. Ginzburg, and A. C. Balazs, "Thermodynamic behavior of particle/diblock copolymer mixtures: Simulation and theory," Macromolecules **33**, 8085–8096 (2000).
[22]Q. Wang, P. F. Nealey, and J. J. de Pablo, "Behavior of single nanoparticle/homopolymer chain in ordered structures of diblock copolymers," J. Chem. Phys. **118**, 11278–11285 (2003).
[23]T. B. Martin, A. Seifpour, and A. Jayaraman, "Assembly of copolymer functionalized nanoparticles: A Monte Carlo simulation study," Soft Matter **7**, 5952–5964 (2011).
[24]S. W. Sides, B. J. Kim, E. J. Kramer, and G. H. Fredrickson, "Hybrid particle-field simulations of polymer nanocomposites," Phys. Rev. Lett. **96**, 250601 (2006).
[25]Q. Y. Pan, C. H. Tong, and Y. J. Zhu, "Self-consistent-field and hybrid particle-field theory simulation of confined copolymer and nanoparticle mixtures," ACS Nano **5**, 123–128 (2011).
[26]V. Pryamitsyn and V. Ganesan, "Strong segregation theory of block copolymer-nanoparticle composites," Macromolecules **39**, 8499–8510 (2006).
[27]L. Meli, A. Arceo, and P. F. Green, "Control of the entropic interactions and phase behavior of athermal nanoparticle/homopolymer thin film mixtures," Soft Matter **5**, 533–537 (2009).
[28]F. Drolet and G. H. Fredrickson, "Combinatorial screening of complex block copolymer assembly with self-consistent field theory," Phys. Rev. Lett. **83**, 4317–4320 (1999).
[29]F. Drolet and G. H. Fredrickson, "Optimizing chain bridging in complex block copolymers," Macromolecules **34**, 5317–5324 (2001).
[30]R. B. Thompson, V. V. Ginzburg, M. W. Matsen, and A. C. Balazs, "Predicting the mesophases of copolymer-nanoparticle composites," Science **292**, 2469–2472 (2001).
[31]R. B. Thompson, V. V. Ginzburg, M. W. Matsen, and A. C. Balazs, "Block copolymer-directed assembly of nanoparticles: Forming mesoscopically ordered hybrid materials," Macromolecules **35**, 1060–1071 (2002).
[32]G. K. Xu and X. Q. Feng, "Position transitions of polymer-grafted nanoparticles in diblock-copolymer nanocomposites," Express Polym. Lett. **5**, 374–383 (2011).
[33]L. Zhang, J. Lin, and S. Lin, "Self-Assembly behavior of amphiphilic block copolymer/nanoparticle mixture in dilute solution studied by self-consistent-field theory/density functional theory," Macromolecules **40**, 5582–5592 (2007).
[34]D. Trombly and V. Ganesan, "Interactions between polymer-grafted particles and bare particles for biocompatibility applications," J. Polym. Sci., Part B: Polym. Phys. **47**, 2566–2577 (2009).
[35]X. M. Zhu, L. Q. Wang, J. P. Lin, and L. S. Zhang, "Ordered nanostructures self-assembled from block copolymer tethered nanoparticles," ACS Nano **4**, 4979–4988 (2010).
[36]X. G. Ye, B. J. Edwards, and B. Khomami, "Morphology tailoring of thin film block copolymers on patterned substrates," Macromol. Rapid Commun. **33**, 392–395 (2012).
[37]Q. Y. Pan, C. H. Tong, Y. J. Zhu, and Q. H. Yang, "Phase behaviors of bidisperse nanoparticle/block copolymer mixtures in dilute solutions," Polymer **51**, 4571–4579 (2010).
[38]K. C. Daoulas, M. Muller, M. P. Stoykovich, S. M. Park, Y. J. Papakonstantopoulos, J. J. de Pablo, P. F. Nealey, and H. H. Solak, "Fabrication of complex three-dimensional nanostructures from self-assembling block copolymer materials on two-dimensional chemically patterned templates with mismatched symmetry," Phys. Rev. Lett. **96**, 036104 (2006).
[39]M. Muller, K. C. Daoulas, and Y. Norizoe, "Computing free energies of interfaces in self-assembling systems," Phys. Chem. Chem. Phys. **11**, 2087–2097 (2009).
[40]M. W. Matsen, F. S. Bates, Block copolymer microstructures in the intermediate-segregation regime," J. Chem. Phys. **106**, 2436–2448 (1997).
[41]I. W. Hamley, K. A. Koppi, J. H. Rosedale, F. S. Bates, K. Almdal, K. Mortensen, "Hexagonal mesophases between lamellae and cylinders in a diblock copolymer melt," Macromolecules **26**, 5959–5970 (1993).
[42]D. A. Hajduk, P. E. Harper, S. M. Gruner, C. C. Honeker, G. Kim, E. L. Thomas, and L. J. Fetters, "The gyroid:- A new equilibrium morphology in weakly segregated diblock copolymers," Macromolecules **27**, 4063–4075 (1994).
[43]M. F. Schulz, F. S. Bates, K. Almdal, and K. Mortensen, "Epitaxial relationship for hexagonal-to-cubic phase-transition in a block-copolymer mixture," Phys. Rev. Lett. **73**, 86–89 (1994).
[44]D. S. Wu, S. J. Paddison and J. A. Elliott, "A comparative study of the hydrated morphologies of perfluorosulfonic acid fuel cell membranes with mesoscopic simulations," Energy Environ. Sci. **1**, 284–293 (2008).
[45]N. F. Carnahan and K. E. Starling, "Equation of state for nonattracting rigid spheres," J. Chem. Phys. **51**, 635–636 (1969).
[46]D. W. Peaceman and H. H. Rachford, "The numerical solution of parabolic and elliptic differential equations," J. Sci. Indust. App. Math. **3**, 28–41 (1955).
[47]V. Eyert, "A comparative study on methods for convergence acceleration of iterative vector sequences," J. Comp. Phys. **124**, 271–285 (1996).
[48]R. B. Thompson, K. O. Rasmussen, and T. Lookman, "Improved convergence in block copolymer self-consistent field theory by anderson mixing," J. Chem. Phys. **120**, 31–34 (2004).
[49]S. Zhu, Y. Liu, M. H. Rafailovich, J. Sokolov, D. Gersappe, D. A. Winesett, and H. Ade, "Confinement-induced miscibility in polymer blends," Nature (London) **400**, 49–51 (1999).
[50]M. W. Matsen, F. S. Bates, "Origins of complex self-assembly in block copolymers," Macromolecules **29**, 7641–7644 (1996).